TITAN'S UPPER ATMOSPHERE FROM CASSINI/UVIS SOLAR OCCULTATIONS

Fernando Javier Capalbo, Yves Bénilan, Roger V. Yelle, Tommi T. Koskinen

TITAN'S UPPER ATMOSPHERE FROM CASSINI/UVIS SOLAR OCCULTATIONS

Fernando J. Capalbo and Yves Bénilan

Laboratoire Inter-Universitaire des Systèmes Atmosphériques (LISA), UMR 7583 du CNRS, Universités Paris Est Créteil (UPEC) and Paris Diderot (UPD), 61 avenue du Général de Gaulle, 94010, Créteil Cédex, France

fernando.capalbo@lisa.u-pec.fr

and

Roger V. Yelle and Tommi T. Koskinen

Lunar and Planetary Laboratory, University of Arizona, 1629 E. University Blvd., AZ 85721, Tucson, USA

Received _____; accepted _____

Submitted to Astrophysical Journal on 2015 July 22.

ABSTRACT

Titan's atmosphere is composed mainly of molecular nitrogen, methane being the principal trace gas. From the analysis of 8 solar occultations measured by the Extreme Ultraviolet (EUV) channel of the Ultraviolet Imaging Spectrograph (UVIS) onboard Cassini, we derived vertical profiles of N_2 in the range 1100 - 1600 km and vertical profiles of CH_4 in the range 850 - 1300 km. The correction of instrument effects and observational effects applied to the data are described. We present CH_4 mole fractions, and average temperatures for the upper atmosphere obtained from the N_2 profiles. The occultations correspond to different times and locations, and an analysis of variability of density and temperature is presented. The temperatures were analyzed as a function of geographical and temporal variables, without finding a clear correlation with any of them; although a trend of decreasing temperature towards the north pole was observed. The globally averaged temperature obtained is (150 ± 1) K. We compared our results from solar occultations with those derived form other UVIS observations, as well as studies performed with other instruments. The observational data we present confirm the atmospheric variability previously observed, add new information to the global picture of Titan's upper atmosphere composition, variability and dynamics, and provide new constrains to photochemical models.

Subject headings: occultations, planets and satellites: atmospheres, planets and satellites: composition, planets and satellites: individual (Titan), techniques: imaging spectroscopy

1. INTRODUCTION

Titan's atmosphere hosts complex organic chemistry processes started by the ionization and dissociation of molecular nitrogen (N_2), which accounts for more than 90% of the atmosphere, and methane (CH_4), the main trace gas with variable abundance of a few percent. Knowledge of the distribution of these constituents with altitude, latitude, and longitude is key to constraining the atmospheric structure and dynamics, and thereby investigating energy and momentum balance in the upper atmosphere. This knowledge is used to develop and constrain models investigating atmospheric chemistry, aerosol production, thermal balance, and escape processes. Therefore, independent, accurate, and precise determination of nitrogen and methane densities in the upper atmosphere is of primary importance.

Several observations and techniques can be used to retrieve the densities of N_2 and CH_4 in the upper atmosphere. One technique uses UV airglow measurements from the Cassini Ultraviolet Imaging Spectrograph (UVIS) (Stevens et al. 2011, 2015). However, these results have a vertical resolution of about 100 km and are dependent on the accurate knowledge of the instrument function and radiometric calibration of UVIS, which has an uncertainty of ∼15% (Stevens et al. 2011). The analysis of airglow data also depends on a complex model of the emission processes of N_2. Another technique uses atmospheric emissions in the infrared. García-Comas et al. (2011) modeled CH_4 emissions and, comparing their model to limb observations performed by the Cassini/Visual-Infrared Mapping Spectrometer (VIMS), derived methane abundances in the range 500 - 1100 km. Again, these results depend on a sophisticated non-local thermodynamic equilibrium model of methane emissions, and are subject to systematic uncertainties that add to the statistical uncertainties in the retrieved profiles. On the other hand, in-situ mass spectrometry, stellar, and solar occultations measured from a spacecraft are the most direct measurements of Titan's neutral upper atmospheric composition, providing a method to directly probe N_2 densities. Several tens of N_2 and CH_4 profiles were measured 'in-situ' by the Cassini Ion and Neutral Mass Spectrometer (INMS) (see for example Waite et al. 2005; Cui et al. 2009; Snowden et al. 2013). The regularity of the close Titan flybys makes this type of observation the most abundant source of information about the densities in the upper atmosphere. Unfortunately,

the spatial spread of the spacecraft trajectory in the atmosphere, together with the variability of the atmosphere, can be a disadvantage when interpreting the profiles in terms of geophysical variables (Mueller-Wodarg et al. 2008). Until recently there were uncertainties about the absolute magnitude of the N_2 densities in the upper atmosphere, with disagreement among values inferred from *in situ* measurements by INMS (Cui et al. 2009; Magee et al. 2009), from accelerometer measurements by the Huygens Atmospheric Structure Instrument (HASI, Fulchignoni et al. 2005), and from the Attitude and Articulation Control System (AACS) on the Cassini spacecraft (Sarani 2009). The fact that the densities from INMS are systematically smaller by about a factor 3 from HASI and AACS pointed to a need to re-calibrate the INMS observations (Teolis et al. 2015).

Cassini/UVIS observes stellar and solar occultations in the EUV, which can be used to measure line of sight absorption by N_2 and CH_4. Kammer et al. (2013) analyzed 4 UVIS/EUV-stellar occultations (flybys T21, T35, T41-I, and T41-II) and determined CH_4 and N_2 atmospheric profiles between 1000 and 1400 km by using an optimized grid search retrieval method. This method allowed them to determine the reduced χ^2 surface of the column densities, and is therefore convenient for estimating their uncertainty, before deriving number densities from them. Stellar EUV occultations, however, are limited by Inter Stellar Medium (ISM) absorption to wavelengths longward of 912 Å, where absorption is by highly complex N_2 electronic band systems (Lewis et al. 2008). These are difficult to interpret at the relatively low UVIS spectral resolution, as all the sharp lines must be modeled before convolution with the instrument function. Moreover, the low stellar flux (compared with the solar flux) leads to relatively low signal-to-noise ratio (S/N).

Solar occultations are a valuable method to retrieve the composition of the upper atmosphere. The first solar occultation by Titan was measured by the UVS instrument (Broadfoot et al. 1977) onboard the Voyager 1 spacecraft. This instrument covers the wavelength range 500 - 1700 Å and has a resolution of 10 Å. Although UVS measured an ingress and an egress occultations, the analysis of Smith et al. (1982) concentrated on the ingress leg because it had better geometrical characteristics. They used the data to confirm that the atmosphere is composed mainly of N_2, with a small abundance of CH_4. Their results were used to constrain several subsequent models of the upper atmosphere (e.g., Yung et al. 1984; Lara et al. 1996; Yelle et al. 1997). A reanalysis of the Voyager solar occultation, utilizing a more sophisticated analysis technique and an improved

model of the instrument (Vervack et al. 2004), solved some inconsistencies noted by Strobel et al. (1992) in the Smith et al. (1982) opacity profiles. Vervack et al. (2004) retrieved number density profiles for N_2, CH_4, and other minor hydrocarbons. They used the continuum N_2 absorption cross section below 650 Å to retrieve molecular nitrogen because the longer wavelength region presenting strong absorption bands was not well known at that time. From the N_2 profiles Vervack et al. (2004) derived a mean thermospheric temperature of 153 K. Cassini/UVIS solar occultations observed in the EUV measure absorption in the ionization and dissociation continuum of N_2 and the dissociation region of CH_4, where cross sections vary smoothly with wavelength and have been precisely measured in the laboratory. Data corresponding to these absorption regions are therefore relatively straightforward to analyze (after the instrument corrections detailed in Section 2) and should provide reliable results. The higher spectral resolution of UVIS compared to UVS allows to better identify and use solar features for the retrieval. A closer observation and better spacecraft stability (except for observations with pointing instabilities) provide better altitude resolution and reduce the corrections needed when processing the data with respect to Voyager 1/UVS. The small spread in latitude/longitude of the observations allows to associate the derived vertical profiles with precise geographical coordinates. Thus, based on a simple technique (when compared with those used to the analysis of Titan's airglow), using well known absorption features, and being independent of calibration, UVIS solar occultations in the continuum region of the absorption cross sections are among the most reliable methods to retrieve local density profiles of N_2, CH_4, and temperatures in the upper atmosphere of Titan.

In this work we present number density profiles of N_2, CH_4, and temperatures in the thermosphere of Titan, retrieved from 8 solar occultations observed by Cassini/UVIS during the flybys T10, T26, T53, T58, T62 (ingress and egress), and T78 (ingress and egress). These observations cover the period from January 2006 to September 2011. The solar occultation from T53 was analyzed by Capalbo et al. (2013), the first published results from UVIS solar occultations. In Section 2 of the present work we detail instrument corrections and data analysis, including a correction of effects of unstable pointing that, if not corrected, would render some of the observations unusable. Section 3 presents the occultations analyzed, including their temporal and spatial coverage. The results are presented in Section 4, followed by a summary

and conclusions in Section 5.

2. UVIS SOLAR OCCULTATION ANALYSIS

A solar occultation occurs when the Sun, as viewed from Cassini, rises from or sets into Titan's atmosphere. This type of observation has been described before (see for example Smith & Hunten 1990; Vervack et al. 2004; Capalbo 2014). From the transmission measured during an EUV occultation, information about the atmospheric composition can be derived for altitudes from 850 to 1600 km, which cover the thermosphere of Titan, near and above the homopause (850 - 1000 km, Vervack et al. 2004; Yelle et al. 2008; Cui et al. 2009). The ionization and dissociation of N_2 and CH_4 happen in this region, where the detection of less abundant molecules is prevented by strong absorption by these species in the UVIS/EUV range (561 - 1182 Å).

The first step in the analysis is to determine the geometric conditions for the observation. The spacecraft trajectory and attitude during the occultation are obtained with the help of SPICE kernels and ICY Toolkit (Acton 1996). Important geometrical information is given in Table 1. The distance from the spacecraft to Titan, the integration duration, and the spacecraft velocity and attitude determine the vertical sampling of the atmosphere. Integration time is 1 s for all solar occultations analyzed here. The distance from the spacecraft to the center of Titan and from the spacecraft to the tangent altitude point range from 10^3 to 10^5 km (the tangent altitude is the shortest distance from the surface of Titan to the line of sight from the spacecraft to the Sun). As a consequence, the vertical sampling varies between approximately 1 km to about 5 km.

In addition to the general steps in the UVIS data analysis described in the Cassini/UVIS User's Guide (LASP 2014) available through the NASA Planetary Data System (PDS), some particular procedures are necessary to analyze UVIS EUV solar occultations. These procedures are described in Capalbo et al. (2013), and thoroughly explained in Capalbo (2014). Thus, we only mention relevant information from these references. It is worth noting that although all the solar occultations have common general characteristics and a common analysis protocol could be established, all present particularities that complicate the study, calling for a detailed case by case analysis. In particular, the position, size, and stability of the image of the source on

the detector. The angular size of in the FOV during the flybys is about 1 mrad. The perceived size of the Sun in the atmosphere level (about 1 - 25 km) is for most occultations bigger than the altitude sampling interval (see Table 1). This oversampling of the atmosphere allows binning the data in altitude (each resulting value being the average of the values in the bin) to improve S/N. The resulting effective sampling of the atmosphere is around 10 - 16 km, depending on the occultation.

2.1. Data Corrections

The most important corrections to the solar port data of the EUV channel are the background subtraction and, for observations with problematic pointing, the wavelength registration. These corrections were performed separately for each of the two spatial lines on the detector containing the solar image, after the onboard binning and before adding the signal in the lines. There are many sources of background. The Radio Thermal Generator background (henceforth BKG1) can be neglected. The present analysis accounts for contributions of photons coming from sources other than the Sun (BKG2), and from light dispersed by the grating (BKG3.1) and by internal reflections (BKG3.2). The contribution of BKG2 was estimated from observations made when all solar light is completely extinguished by atmospheric absorption (altitudes $\lesssim$ 300 km), giving for all occultations a negligible contribution at a rate of a few 10^{-2} counts sec^{-1} pixel^{-1}. Although the exact source, spectral and time variation of the scattered light contribution (BKG3.1 and BKG3.2) are unknown, the spectral and temporal characteristics of the data reveal the presence of at least two distinct contributions. The first varies with time in the same manner as the count rate at the long wavelength end of the spectrum. This can be seen in Figure 1, showing light curves from the T53 occultation for bins around solar lines at 584 Å and 630 Å, and for a bin covering the range 1100 - 1160 Å. For altitudes below ∼1000 km, the light curve for the short wavelength bins show background counts that vanish in a similar fashion to that of the counts in the long wavelength bin. It was therefore hypothesized that this background is due to light scattered by the instrument from longer wavelengths. We corrected it following the procedures described in Capalbo et al. (2013); Capalbo (2014). The second manifestation of the scattered

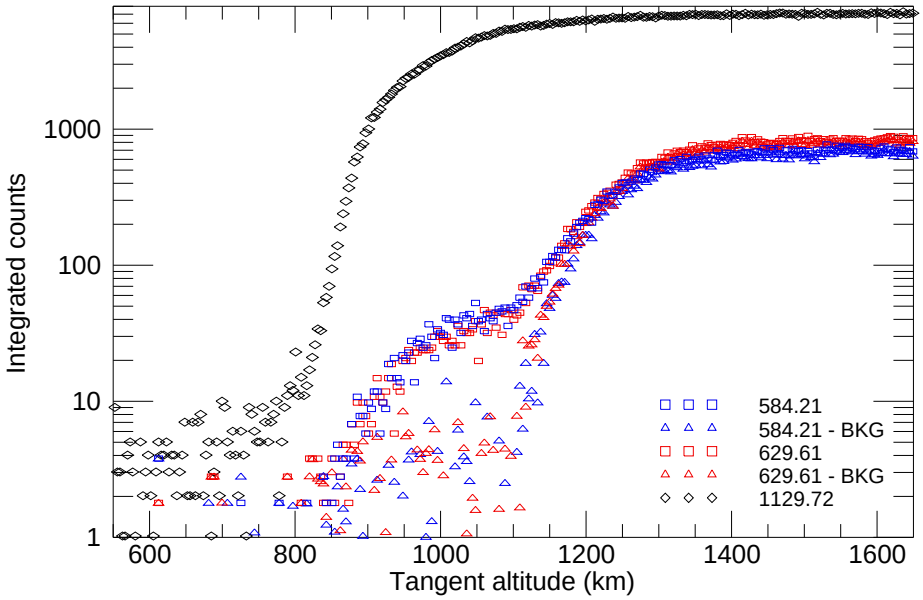

Fig. 1.— Light curves for 7-band bins centered in two solar lines before (□) and after (△) the BKG correction. Light curve for a 100-band bin in the long wavelength end of the detector (◇) used as proxy for one of the sources of BKG. The wavelengths corresponding to the center of the bins are shown in the plot, in Å. The data are from the T53 flyby.

light is in the form of residual background evident next to the measured solar emission lines. Interpreted as extended wings of the instrument Point Spread Function (PSF), its temporal behavior is the same as that of the emissions features themselves. It had no effect on the analysis, so it was not subtracted. The corrected light curves for bins around 584 Å and 630 Å are shown in Figure 1.

A wavelength re-calibration was also necessary. Even when the Sun remained within the limits of the FOV for all the occultations, the Sun could be imaged off the slit center in the dispersion or spatial direction, and it could drift further during the observation due to pointing instabilities — examples of the calculated positions and sizes of the Sun in the FOV, in a case of good pointing (flyby T58) and in a case of bad pointing (flyby T62) are shown in Figure 2. This resulted in spectra suffering from a wavelength- and time-dependent shift with respect to the calibration provided in the PDS archive. This shift is significant for 4 of the 8 occultations analyzed here (see Section 3). Based on the position of well known and strong solar emission

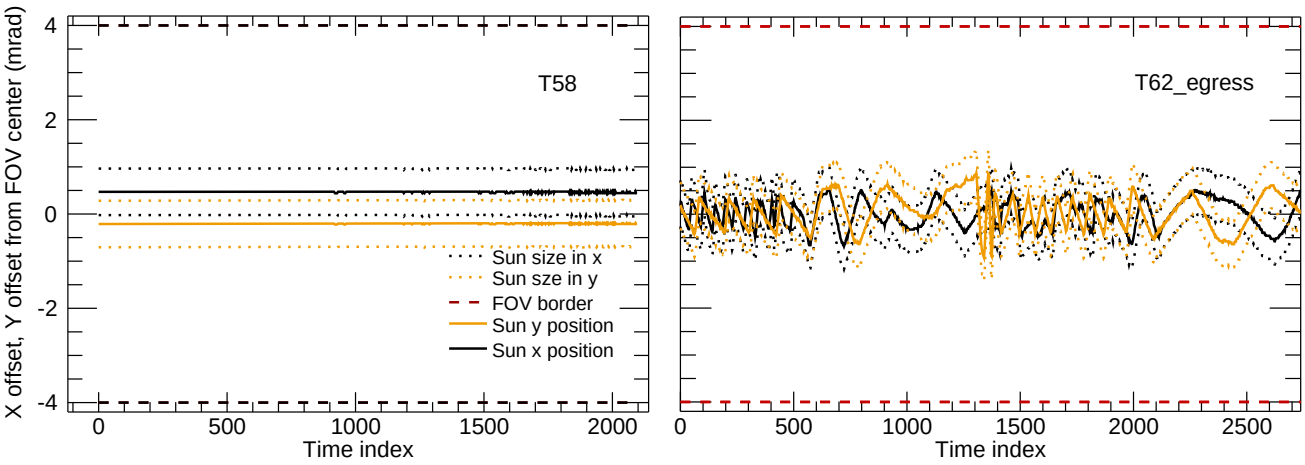

Fig. 2.— Sun position (solid lines) and size (dotted lines) in the across slit (X) dimension and along slit (Y) dimension of the squared FOV of the UVIS solar occultation port, for occultations T58 and the egress leg of T62. The difference time ranges are a consequence of the different duration of the occultations.

lines, a re-calibration of all measured spectra was performed. The drift of the solar image in the detector led to significant variations in the light curves as the flux of a solar emission line moved from one wavelength band to the other over time (see the top right panel of Figure 3). These UVIS bands were identified in the UVIS spectra as the center of a Gaussian fitted to the emission line. An example of this is shown in the bottom plots of Figure 3, showing the UVIS/EUV band corresponding to 629.61 Å as a function of time, for detector line 5. As the movement of the spacecraft that originated the pointing drift is expected to be smoother than the oscillations observed, the data was smoothed as shown by the trend line in the plot (green solid line). For the lower altitudes, where the reference solar lines were absorbed, a quadratic extrapolation of the behavior at the higher altitudes was used. Once the position of the reference lines in terms of UVIS bands was determined, a wavelength calibration polynomial of second order was derived for each altitude. The measured wavelength shift for the reference lines vary from one occultation to the next, being 3.2 Å ($\sim$ 5 pixels) in the worst case. The residual i.e., the difference between the wavelengths of the reference solar lines and the corrected wavelengths of the lines in the data, is up to 0.4 Å in the worst case, but less than 0.2 Å for most cases. This reflects the accuracy of the wavelength re-calibration, which is about 1/3 of an EUV wavelength band.

The top plots in Figure 3 show the light curves before and after background and wavelength correction for the UVIS/EUV band 113 (corresponding to 629.61 Å), for a stable (T53) and an unstable (egress leg of T62, henceforth $T62_{egress}$) occultation. In the case of T53, no perturbation

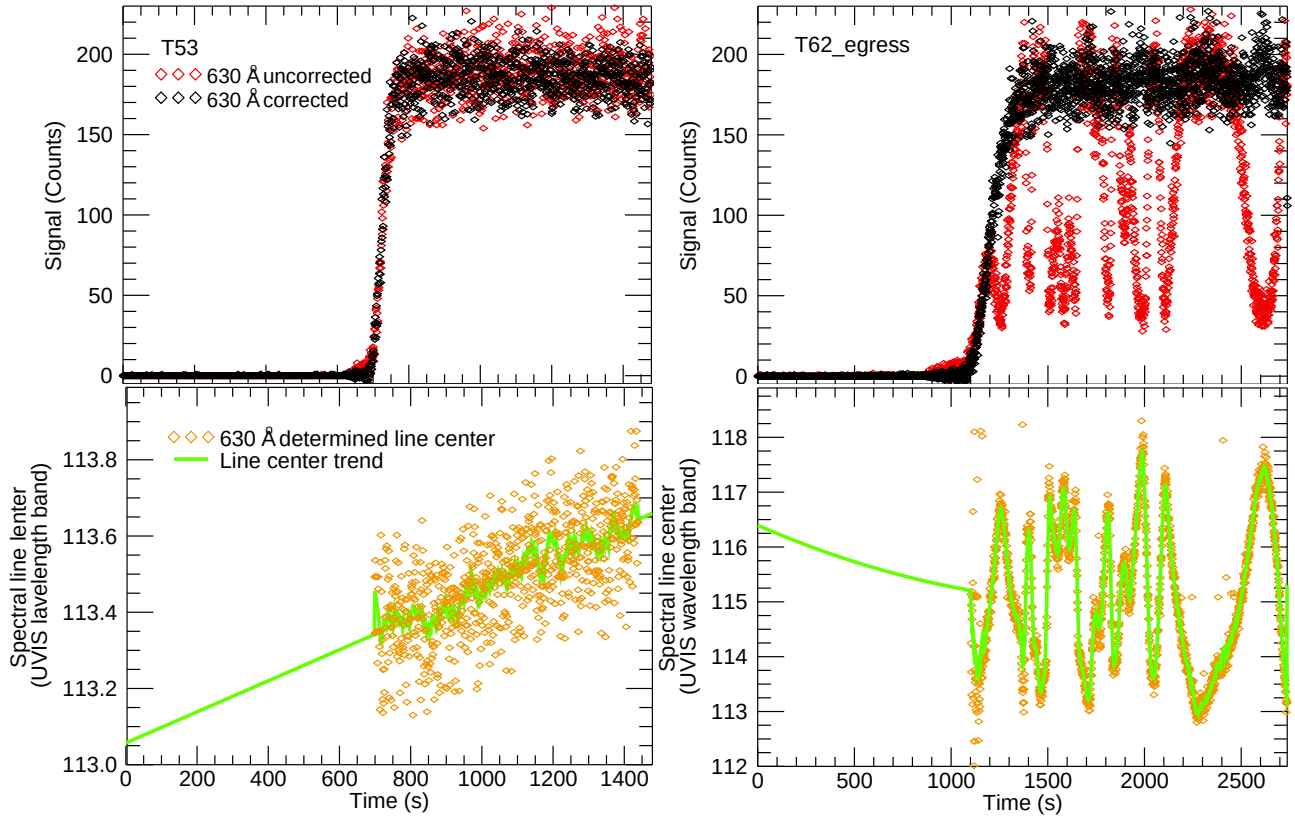

Fig. 3.— Top: Light curves before and after background and wavelength correction for UVIS/EUV band 113, corresponding to 629.61 Å (representative of a solar emission line). Bottom: UVIS/EUV band corresponding to the 629.61 Å emission line center (as determined from the Gaussian fits, see text), for detector line 5, as a function of observation time. The plots on the left and right correspond to the T53 and egress leg of T62 solar occultations, respectively.

is clear from a visual inspection of the light curves, but the analysis shows a small, sub-pixel wavelength shift. For the unstable occultation the light curve is clearly corrupted by the shift. It has to be kept in mind that each observation has its own characteristics and these methods are more or less effective in each case. In cases with very bad pointing, one could wonder if the wavelength correction results in an acceptable light curve. This was confirmed by analyzing the statistics of the light curve above the Top Of the Atmosphere (TOA) for 2 of the most affected

occultations (T26 and T62$_{egress}$). Figure 4 shows the histogram of counts measured outside the atmosphere in the bins used for the analysis of absorption (582.40 - 586.03 Å, 627.79 - 631.43 Å, and 1082.73 - 1087.58 Å), after the data corrections, for these 'worse case' occultations. The histograms for a stable occultation (T58) are also shown for comparison. The similarity of

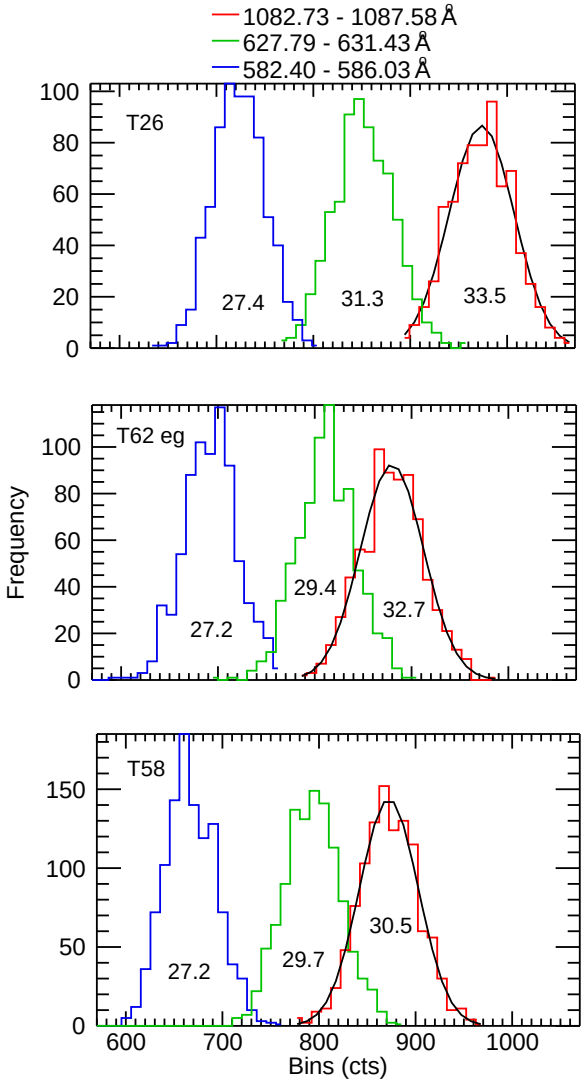

Fig. 4.— Count statistics above the atmosphere for the spectral bins shown at the top of the plot, for observations during flybys T26, T62$_{egress}$, and T58, after data corrections. The numbers in the plots are the standard deviations of the fitted Gaussians, one of which is shown as example in each plot.

the histograms shows that the corrected light curves present similar statistics as those from an occultation with stable pointing. The re-calibration procedure not only confirms the correlation

of the fluctuations in the light curve with the shift of the line center in the detector—which also correlates with the pointing drifts shown in Figure 2—but also efficiently corrects the light curves.

2.2. Atmospheric Absorption and Analysis Methods

Nitrogen and methane are the main EUV absorbers in Titan's atmosphere. Nitrogen, by far the dominant atmospheric constituent, absorbs photons in the region 561 - 1000 Å. Methane has a wider absorption region (561 - 1450 Å in UVIS/EUV,FUV ranges), and absorbs most photons in the remaining 1000 - 1450 Å wavelength range (see for example Lavvas et al. (2011) for a detailed description of N_2 and CH_4 absorption). The less energetic photons penetrate deeper into the atmosphere and can be absorbed by minor species (Koskinen et al. 2011). The Sun was assumed to have a steady output during the occultations. The EUV spectrum of the Sun consists of a weak continuum intercepted by intense emission lines. We retrieved density profiles of N_2 and density profiles of CH_4 by using two bins centered on the solar He I line at 584 Å (582.40 - 586.03 Å) and the O V line at 630 Å (627.79 - 631.43 Å), and a bin spanning solar lines around 1085 Å (1082.73 - 1087.58 Å), respectively. The retrieval procedure to calculate column densities and number densities is explained in Capalbo et al. (2013); Capalbo (2014). It takes advantage of the facts that CH_4 dominates absorption in the long wavelength bin, that N_2 dominates absorption in the short wavelength bins (although a CH_4 contribution is still important and accounted for, Capalbo et al. 2013; Capalbo 2014), and that the cross sections do not change significantly in the wavelength bins used. The procedure allowed us to retrieve abundances without using the complicated band structure in the N_2 absorption cross section, where the cross section varies by several orders of magnitude in narrow lines (Lewis et al. 2008). The N_2 absorption cross sections used for the calculations are from Samson et al. (1987), measured with a band-pass of 1 to 3 Å; the CH_4 absorption cross sections used are from Kameta et al. (2002), with resolution of 1 to 4 Å and measured at 298 K. The absorption cross sections have an uncertainty of $\sim 3\%$.

The column density profiles were limited in altitude before the number density calculations. Column densities calculated for altitudes with very low, or too high absorption are affected by noise, background, and other measurement effects, and do not represent the real state of the

atmosphere. To limit the profiles, the valid altitudes for a particular profile were defined as those for which the transmission in the wavelength bin used for the retrieval satisfied:

$$T + \sigma_T < 0.99 \qquad and \qquad T - \sigma_T > 0.01, \tag{1}$$

where T and σ_T represent the transmission and its uncertainty, respectively. Nevertheless, values at the extremes of the resulting profiles deserved a special attention. Some values at the lowest altitudes in some of the nitrogen profiles seem to be too small, which could be due to residual background contamination not eliminated by the corrections described above. At the highest altitudes, the column densities showed a big dispersion and uncertainties. Moreover, at these high altitudes, the CH_4 contribution to the absorption at short wavelengths, used to correct the measured N_2 optical depth, is calculated using extrapolated CH_4 number densities (see Capalbo et al. 2013; Capalbo 2014), and therefore the resulting N_2 column densities are less precise. Thus, column densities with uncertainties bigger than 100% at the top of the profiles were excluded. The only exception was the profile calculated from the 584 Å bin for T26, values at 1492, 1508, and 1541 km had uncertainties bigger than 100% but were not the upper most values in the profile. Thus they were interpolated, assuming a decreasing exponential behavior as a function of altitude. This was done to keep as many high values as possible, and because the spatial inversion routines need a column density profile without missing values.

The retrieved number densities are very sensitive to oscillations in the column density profiles. After the regularized inversion, altitudes for which the inversion routine failed, resulting in negative number densities or with uncertainties bigger than 100%, were excluded from the profiles. This happened for only a few altitudes in the high end of the profiles. Values within one resolution width from the top of the profiles were eliminated, to avoid border effects due to the second derivative operator used in the inversion (Capalbo 2014). The N_2 number densities shown in Section 4 were calculated as the mean of the number densities derived from each bin involved in the analysis (centered in 584 Å or in 630 Å) for altitudes where the number densities overlapped. For altitudes with results from only one bin, this value was taken as the number density for that altitude. The different altitudes in the number density profile have similar, but different altitude resolutions, determined by the altitude sampling and the width of the averaging kernels of the inversion (see for example Capalbo et al. 2013). The median of the resolutions was calculated

as a characteristic resolution for the whole profile. The resolution for the average N_2 profile was calculated as the average of the resolutions of the profiles derived from the individual bins.

The N_2 number density profiles were used to derive temperature in the upper atmosphere of Titan. Nitrogen is relatively inert and, due to its dominance in the upper atmosphere, its average temperature can in general be regarded as a good indicator of the average temperature of the atmosphere as a whole. The procedure used to derive temperature is based upon the assumptions of a hydrostatic, diffusive and isothermal upper atmosphere. Under these assumptions, the temperature can be calculated from an effective scale height of the atmosphere, obtained from a linear fit to the natural logarithm of the measured number densities. This method has been used before to derive temperatures from INMS measurements (Cui et al. 2009; Westlake et al. 2011). We derived temperature from the N_2 profile calculated as the mean of the number density profiles derived from each bin involved in the analysis (centered in 584 Å or in 630 Å). To avoid systematic uncertainties coming from values in the borders of the profiles (see comments on column densities above), the calculations were limited to altitudes for which the transmission in the wavelength bin used to retrieve the profile was between 0.1 and 0.9. In the rare cases when the altitudes were different for the two bins, the lower altitude between the two upper limits, and the higher altitude between the two lower limits were kept. The observation $T62_{egress}$ is an exception. As the spacecraft was inside the atmosphere during part of the observation (see Section 3) the number densities are underestimated, especially for the highest altitudes, for which Cassini was deeper into the atmosphere. We therefore present two temperatures for this flyby. A lower limit for the temperature was calculated as for the other occultations, using the N_2 profile limited to the range 1144 - 1319 km. The other temperature was calculated using the profile from the lowest altitude retrieved up to 1144 km. For this observation, the densities at these low altitudes seem to be not affected by the issues mentioned above, and were therefore used to determine a 'low altitude temperature'. Unless otherwise stated, it is this 'low altitude temperature' that is referred to when the temperature from this observation is considered.

We evaluated the uncertainty of the mean temperature by using a Monte Carlo technique. For each occultation we simulated 40000 number density profiles. For each simulated profile the number density for each altitude was drawn from a normal distribution with mean equal

to the value in the retrieved profile, and standard deviation equal to the retrieved uncertainty. The uncertainties used for the simulated profiles were equal to the retrieved uncertainties. The reported temperatures and uncertainties are obtained from the mean and standard deviation of the temperatures obtained from the simulated profiles. The Monte Carlo analysis was also performed with the individual profiles derived from the two short wavelength bins, and a temperature was calculated as the mean of those derived from each profile. The results were consistent with those obtained averaging the profiles and then calculating temperature.

3. UVIS OCCULTATIONS ANALYZED

We analyzed solar occultations through Titan's atmosphere measured with the UVIS/EUV channel that took place during flybys T10 through to T78. The data are available on the PDS database. Geographical and other ancillary information about the solar occultations analyzed in this work is presented in Table 1. When a range of values is given, the values are sorted by increasing time of observation.

This final list merits some comments. In some cases an ingress occultation and an egress occultation were measured during the same flyby. This is the case of T10, T62 and T78. The ingress leg of T10 is unusable, the spacecraft was inside the atmosphere while the occultation took place and the light curves are not appropriate for the analysis. The egress leg of T10 will therefore be simply referred to as T10. The spacecraft was also inside the atmosphere during part of the egress occultation that took place during the T62 flyby ($T62_{egress}$). Cassini's altitude was lower than 1500 km for tangent altitudes between approximately 1025 and 1450 km, passing by the tangent altitude point when the tangent altitude was around 1350 km. Nevertheless, the resulting light curves were suitable for analysis, and abundances could be derived. Obviously, as the line of sight did not probe the whole atmosphere, the abundances derived should be considered lower limits. The abundances at low altitudes, however, measured when Cassini was just entering the atmosphere, are expected to be less underestimated than those at high altitudes.

Observations during T10, T26, and both observations during T62 suffered from pointing instabilities causing wavelength shifts. In these cases the wavelength re-calibration procedure,

Table 1. Characteristics of solar occultations analyzed.

Flyby	Data product (EUVyyyy_doy_hh_mm)	Lat. [a] (deg)	Lon. [a] (deg W)	LST [b] (hh:mm)	SLT [b] (hh:mm)	Altitudes probed (km)	Original sampling [a] (km)	Sun diameter in atm. [a] (km)	Min. distance [d,a] (km)	T (K)
T10	EUV2006_015_11_25	-62 – -54	0 – 11	20:04	08:31	0 – 5365	2.6 – 2.9	9.7 – 11	9513	163 ± 2
T26	EUV2007_069_01_05	-76 – -77	41 – 29	23:10	13:47	10185 – 0	5.4 - 5.3	5.7 - 5.4	5293	139 ± 5
T53	EUV2009_110_00_11	-21 – -29	237	18:03	22:02	0 – 4802	3.9 – 4.3	5.1 – 4.7	4782	154 ± 5
T58	EUV2009_189_15_42	87 – 85	240 – 237	17:40	21:47	6663 – 0	3.2	12 – 11	10994	113 ± 4
T62_eg	EUV2009_285_08_15	-68 – -61	48 – 49	06:08	21:35	0 – 2432	1.1 – 0.9	2.7 – 0.3	0	179 ± 9 [c]
T62_in	EUV2009_285_06_27	2 – -5	230	17:59	21:31	5937 – 0	1.3 – 1.2	26 – 23	23108	172 ± 2
T78_eg	EUV2011_255_02_23	25 – 20	354 – 352	05:41	17:32	0 – 7914	4.8 – 5.0	7.4 – 7.2	7450	160 ± 5
T78_in	EUV2011_255_02_23	28 – 32	162 – 161	18:25	17:31	4021 – 0	5.0 – 4.8	9.4 – 9.2	9528	121 ± 3

[a]For altitudes relevant to CH_4 or N_2 absorption.

[b]ST:Titan's Local Solar Time. SLT: Saturn Local Time. For the half light point in the light curve of the bin around 584 Å.

[c]ow altitude value.

[d]Spacecraft - tangent altitude minimum distance.

described in Section 2.1, allowed for the data to be corrected and column densities could be retrieved as usual. Although flybys T53, T58 and T78 were more stable and the correction was not critical, the wavelength correction was still performed to improve the quality of the data. The solar occultation measured during flyby T32 presented pointing instabilities that could not be corrected with the procedures use in this work, therefore no abundances were derived from it.

The geographical coordinates for relevant altitudes (in terms of absorption) of all the observations analyzed are summarized in Figure 5. The coordinates of the T53 UVIS/FUV-stellar

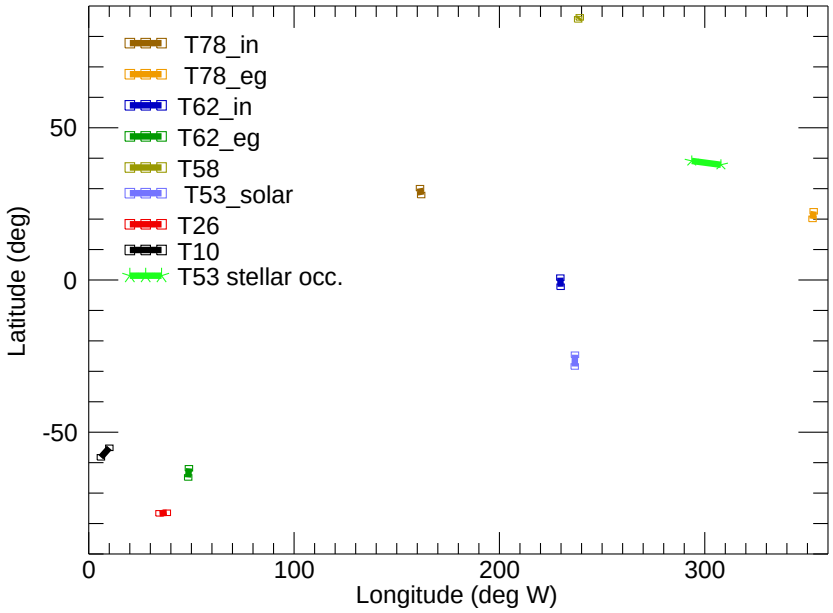

Fig. 5.— Latitude and Longitude for all the observations analyzed.

occultation (Koskinen et al. 2011) is also shown. Although the latitude coverage is sparse, the occultations probed low, mid and high latitudes in both hemispheres. There are, however, gaps in the sampling, most of the occultations accumulating in low/mid latitudes on both hemispheres and longitudes above 150° W, or in high southern latitudes and longitudes below 100° W. The solar occultations also probe different longitudes, leaving big gaps for the longitude range 50 - 150° W and for the range 250 - 350° W. Most of the solar occultations took place at the evening terminator, only 2 took place at the morning terminator. None of them took place while Titan was positioned from Saturn midnight to Saturn sunrise times.

4. RESULTS AND ANALYSIS

Figures 6 and 7 show the CH_4 and N_2 number densities, respectively. The profiles from

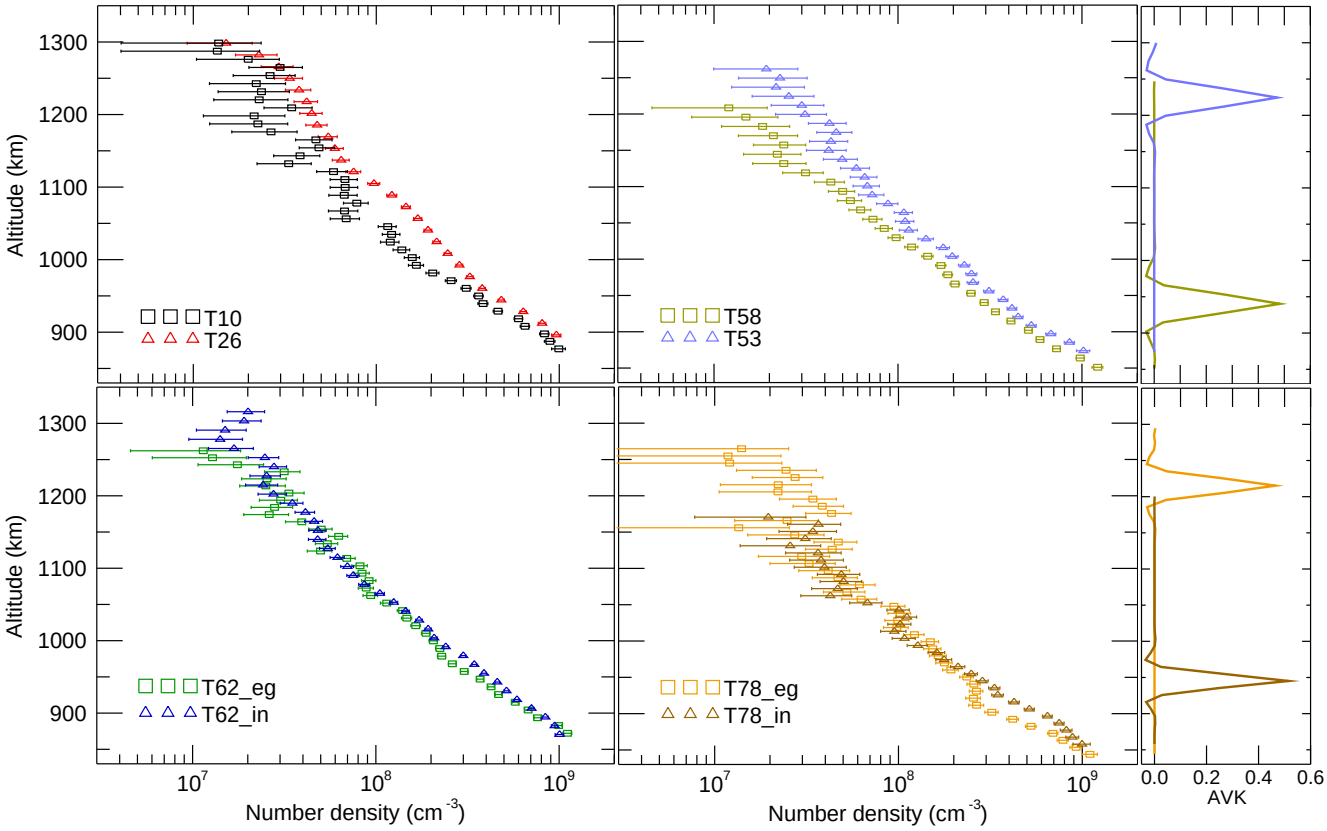

Fig. 6.— Methane number density profiles derived from the solar occultations analyzed. Densities from $T62_{egress}$ above 1025 km should be interpreted as lower limits. On the right, as an example, AVK for some altitudes, and for four of the profiles: T53, T58, $T78_{ingress}$, $T78_{egress}$.

T53 were first presented in Capalbo et al. (2013). Most of the profiles present oscillations. Atmospheric waves have been proposed to explain oscillations observed in CH_4 and N_2 density profiles from Titan (see for example Koskinen et al. 2011; Snowden et al. 2013). The oscillations in our results, especially those oscillations within a few tens of km, should be interpreted with caution as they might be due to divergences from the real profile caused by the noise in the column densities, not smoothed by the regularization procedure. The spacecraft was inside the atmosphere during part of $T62_{egress}$ (see Section 3). Therefore, the number densities, especially in the upper part of the profiles, are underestimated and should be interpreted as lower limits.

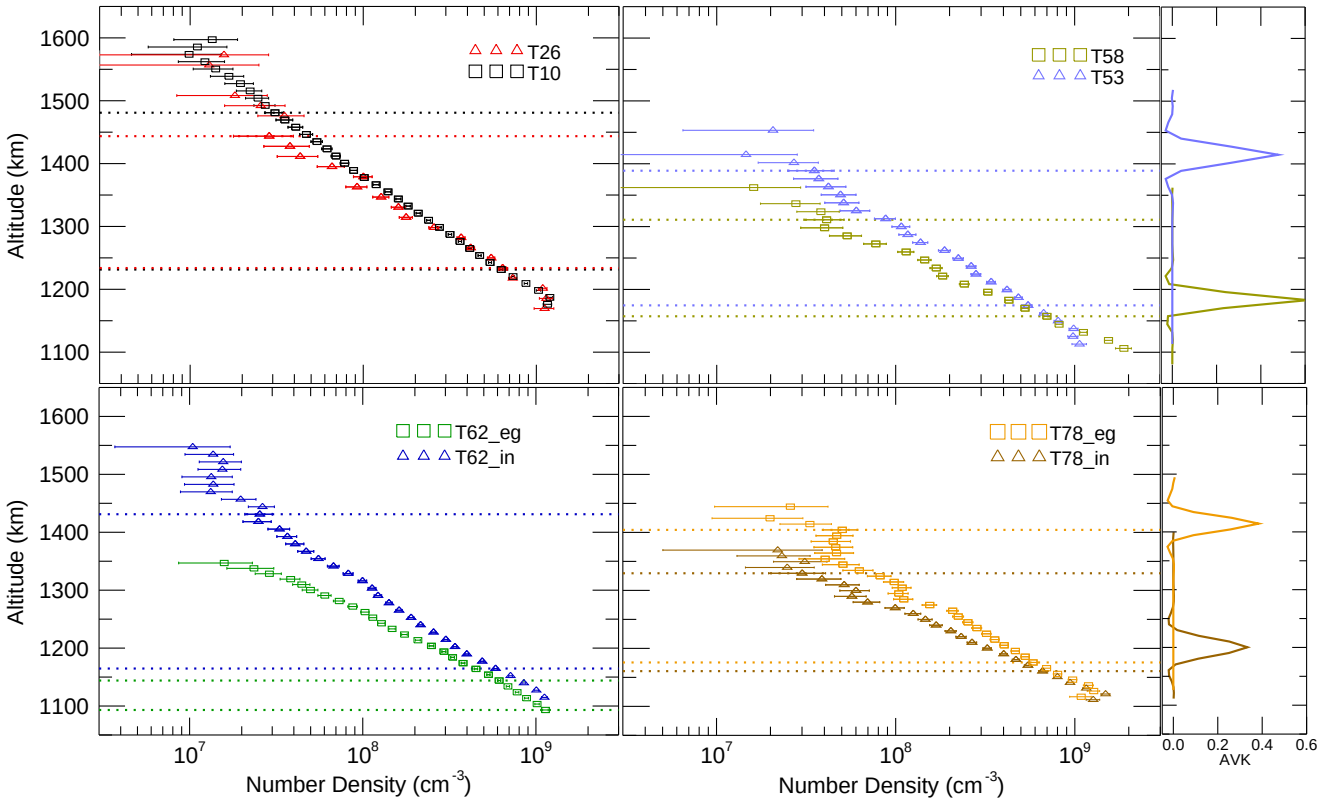

Fig. 7.— Nitrogen number density profiles derived from the solar occultations analyzed. Densities from $T62_{egress}$ should be interpreted as lower limits. The horizontal dotted lines show the altitude range used to derive temperature. On the right, as an example, AVK for some altitudes, and for four of the profiles: T53, T58, $T78_{ingress}$, $T78_{egress}$.

The altitude resolution of the profiles vary from one observation to the other. The resolution associated with the CH_4 number densities is about 20 km for T10, $T62_{egress}$, $T78_{egress}$, and $T78_{ingress}$, about 30 km for T53, T58, and $T62_{ingress}$, and about 50 km for T26. The resolution associated to the N_2 number densities is about 20 km for T26 and T58, about 30 km for T53, $T62_{egress}$, $T62_{ingress}$, $T78_{egress}$, and $T78_{ingress}$, and around 50 km for T10. The final altitude resolution depends on the width of the averaging kernels (AVK). Averaging kernels for particular altitudes are shown in Figures 6 and 7, as an example, for four of the occultations: T53, T58, $T78_{ingress}$, $T78_{egress}$. The AVKs for N_2 correspond to the profiles derived from the 584 Å bin.

4.1. Number Density Variability

In the context of the variability observed in Titan's thermosphere (see e.g. Magee et al. 2009; Snowden et al. 2013), it is interesting to analyze the behavior of the number densities measured. The solar occultation data confirm the variability observed in the upper atmosphere by other instruments, and are consistent with the decrease in densities over time observed in the INMS data. Even for profiles derived from one flyby but different occultations (e.g. T78), the profiles are clearly different.

Aiming at a quantitative analysis of variability, we concentrated on the number densities measured at 1250 km for N_2 and at 900 km and 1170 km for CH_4. Table 2 shows statistics for the number densities corresponding to the altitudes in the profiles closest to the altitudes mentioned above. The high altitude value in the profile of methane from $T62_{egress}$, and the profile of nitrogen from the same flyby were not considered for the analysis of variability. The values in Table 2 indicate that the relative dispersion measured for nitrogen is more important than that measured for methane, and that the relative dispersion of methane sampled at low altitude is smaller than that sampled at high altitude. It has to be taken into account, however, that the different locations and times corresponding to the different observations are blended in this statistics.

Figure 8 shows the number densities for the selected altitudes, plotted as a function of time. In both the CH_4 and the N_2 data sets there is an overall tendency of decreasing abundance with time. The steepest decrease as a function of time is that of the values sampled at 900 km in the CH_4 profiles. It is worth noticing, however, that different locations are blended in this plot.

Table 2: Number Density Statistics.

Species	N_2	CH_4	
Altitude (km)	1250	900	1170
Median (x$10^7 cm^{-3}$)	22	68	4.6
Mean (x$10^7 cm^{-3}$)	28	68	3.7
Std. Dev. (x$10^7 cm^{-3}$)	16	20	1.5
Std. Dev./Mean	0.58	0.30	0.40

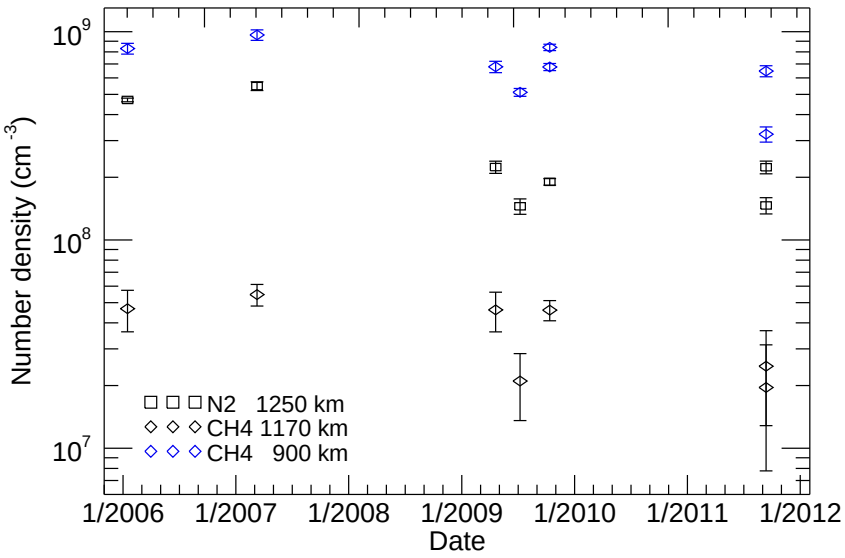

Fig. 8.— Methane number densities and nitrogen number densities versus time, for the three different altitudes shown in the plots.

A downward general trend of the N_2 densities during the Cassini mission has been observed by Westlake et al. (2014). In they analysis of INMS data from the TA-T95 flybys the highest densities observed were measured during the TA and T5 encounters and the lowest densities observed late in the mission. Snowden et al. (2013), in their analysis of INMS data from the T5-T71 flybys, observed that the median temperature in the upper atmosphere decreased after flyby T32, which took place in June 2007. This correlates with the decrease in N_2 densities in the present data set after T26, which took place in March 2007. Nevertheless, considering the limited sampling in the present work, the overlapping of uncertainties at high altitudes, and the oscillations in the density profiles, the trends described at the different altitudes should be interpreted with caution.

4.2. Methane Mole Fraction

An important contribution of this work is the derivation of N_2 number density profiles and CH_4 number density profiles for the same time and location in the upper atmosphere. This allows for a straightforward determination of the vertical profile of the CH_4 mole fraction, an important quantity characterizing the dynamics of the atmosphere, and often considered in the

models. The mole fraction (shown in Figure 9) was calculated as the ratio between the methane number density and the sum of the methane number density and the nitrogen number density, the mayor constituents of the atmosphere. The calculation was limited to the altitudes that were used to determine temperatures (as explained in Section 2.2) and are shown between dotted lines in Figure 7. Our results support the observations of variability and differences in dynamics

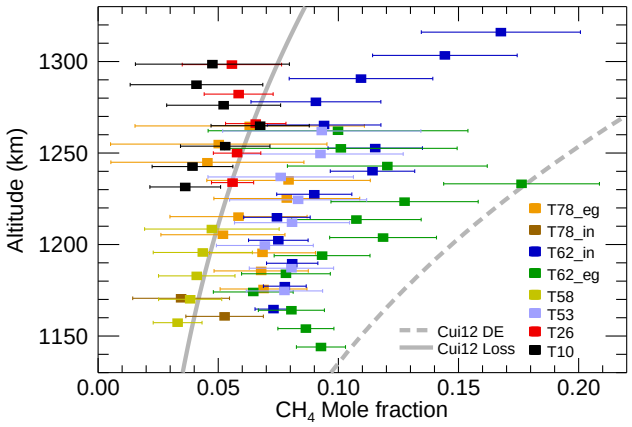

Fig. 9.— Methane mole fraction derived from all solar occultations analyzed. The gray line (Cui12 Loss) represents a model with a loss rate of $3.8 \times 10^{27} s^{-1}$, the blue line (Cui12 DE) represents a diffusive equilibrium model, both from Cui et al. (2012).

revealed by the study of Cui et al. (2012). These authors thoroughly revisited the CH_4 structure in Titan's upper atmosphere, combining Cassini/INMS data from 32 flybys and incorporating several updates in the data reduction algorithms. After fixing the eddy mixing profile on the basis of the ^{40}Ar mole fraction, they used the methane mole fraction derived from INMS data to constrain the methane escape rate in their model. They found that the considerable variability in CH_4 structure among different flybys implies that methane escape on Titan is more likely a sporadic rather than a steady process, with the CH_4 profiles from about half of the flybys showing evidence for strong escape and most of the other flybys consistent with diffusive equilibrium. Considering the globally averaged CH_4 mole fraction, the best fit to the data was obtained with a model using an escape rate of $3.8 \times 10^{27} s^{-1}$. This model profile is shown in Figure 9 (solid line), together with the one corresponding to diffusive equilibrium conditions (dashed line). The mole fractions derived from UVIS occultations are all below the diffusive equilibrium model profile, and most are between the two models, thus confirming the variability of methane escape.

Westlake et al. (2014) presented CH_4 mixing ratios derived from Cassini INMS observations of Titan's atmosphere from the TA-T95 flybys, which took place from 2004 to 2013. The CH_4 mixing ratio showed a declining trend from mid-2006 to roughly 2008, followed by an upward trend during the extended solar minimum from 2008 to sometime in 2010. This was followed by a downward trend in the mixing ratios of CH_4 after the onset of solar maximum conditions in 2011. Comparing observations from different flybys and through modeling studies using the time-dependent Titan Global Ionosphere-Thermosphere Model, Westlake et al. (2014) argued that this trend is due to enhanced photodestruction of CH_4 in Titan's thermosphere from the increased solar EUV/UV flux during solar maximum times. The trends observed by Westlake et al. (2014) are not evident from our methane mole fractions. However, our data set is sparse, and our uncertainties big, preventing any firm conclusion about the temporal variation of the methane mixing ratio. On the other hand, most mole fractions derived from UVIS data correspond to locations and times not covered by INMS data, and can therefore serve as additional constraints in studies of the methane structure.

4.3. Comparison with Other Measurements of Abundance

The CH_4 densities and the N_2 densities from UVIS solar occultations presented here complement the measurements from other instruments (like INMS and UVS), and measurements from other UVIS observations. Capalbo et al. (2013) showed a synergy between UVIS/EUV-solar and UVIS/FUV-stellar occultations observed during flyby T53, when the different occultations provided a measurement of methane number densities at two different, well defined, geographical coordinates within a time span of some hours. Kammer et al. (2013) analyzed 4 UVIS/EUV-stellar occultations (flybys T21, T35, T41-I, and T41-II) and derived CH_4 and N_2 number density profiles between 1000 and 1400 km. The profiles correspond mainly to low/mid latitudes and the last three fall between those from flybys T26 and T53, presented here. In Figure 10 we compare the profiles of methane and nitrogen derived from the UVIS/EUV-stellar occultation during T21, with those we derived from the UVIS/EUV-solar occultation during T26, which took place 88 Earth days later, and further south. Table 3 presents temporal and geographical information

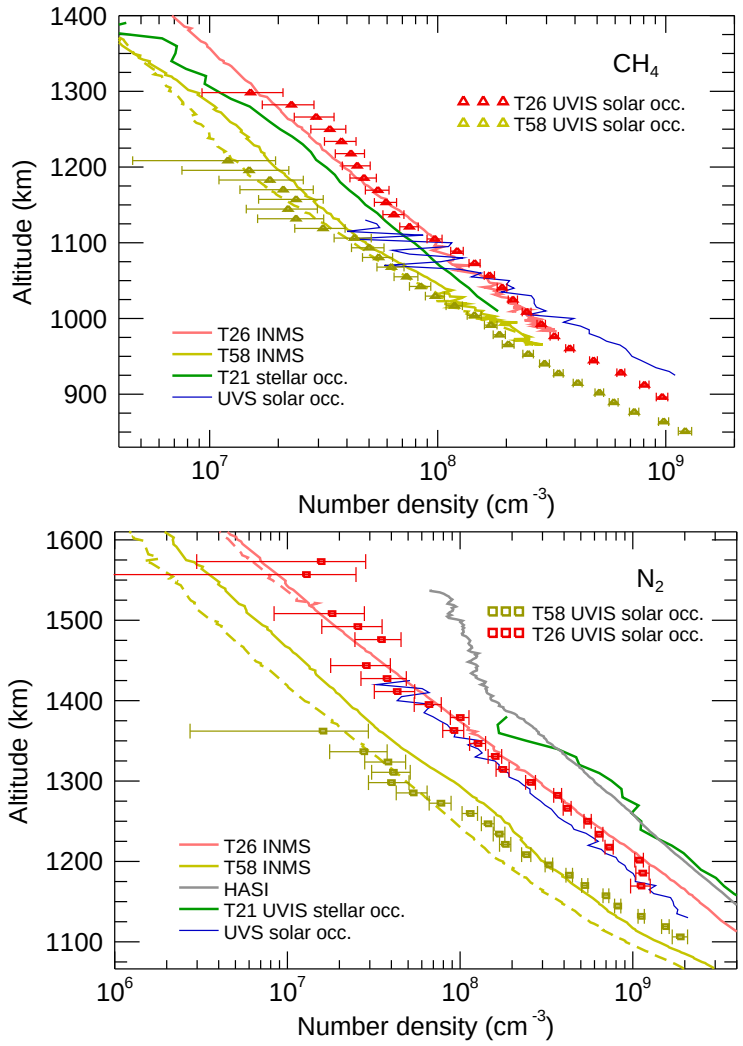

Fig. 10.— Methane (top) and nitrogen (bottom) number density profiles derived from solar occultations T26 (in March 2007) and T58 (in July 2009). Also shown are the profiles for both species measured by UVIS/EUV during a stellar occultation in December 2006 (Kammer et al. 2013), profiles measured by UVS onboard Voyager 1 during a solar occultation in November 1980 (Vervack et al. 2004), the profiles from INMS (inbound: solid line, outbound: dashed line) measured during T26 and T58 (Snowden et al. 2013), and a nitrogen profile calculated from the density measurements performed by the HASI instrument during the Huygens probe descent through Titan's atmosphere in January 2005 (Fulchignoni et al. 2005).

for the data in Figure 10. The UVIS/FUV-stellar methane profile from T21 falls below the UVIS/EUV-solar profile measured for T26, the FUV-stellar nitrogen profile from T21 is above the EUV-solar profile measured for T26.

The optimal measurement conditions for INMS and UVIS are different so it is uncommon to have both type of measurements in the same flyby. However, INMS performed measurements of N_2 and CH_4 during flybys T26 and T58. The profiles from the inbound and outbound legs of these flybys are compared with the UVIS solar occultation results in Figure 10. The INMS densities shown were multiplied by the revised calibration factor of 2.2 (Teolis et al. 2015). Assuming no instrumental artifacts or systematic errors, the differences between UVIS and INMS, both measurements corresponding to the same flyby, can be due to spatial variations in the atmosphere. Comparisons of UVIS/EUV-solar occultation results for T53 with INMS, UVS and HASI results were presented in Capalbo et al. (2013). There, the T53 CH_4 densities and N_2 densities are compared with corresponding INMS results from the inbound and outbound passes in flybys T51 and T55, that took place about one month before and after T53, respectively. The UVIS/EUV results broadly agreed with most of the results from previous work presented in Capalbo et al. (2013), within factors 1-3 (1-1.8 for comparisons with INMS results). Capalbo et al. (2013) scaled the INMS densities by a factor 2.9 from the original calibration. Using the revised correction factor (Teolis et al. 2015) for the INMS results, makes the UVIS profiles and the INMS profiles in Capalbo et al. (2013) agree within factors 0.8-1.4. The restricted sampling of the available data did not allow the authors to reach a firm conclusion on horizontal/seasonal variations.

Also shown in Figure 10 are the N_2 density profile derived from the Huygens Atmospheric Structure Instrument (HASI) mass profile (Fulchignoni et al. 2005), assuming an atmosphere composed of nitrogen and 5% of methane; and the N_2 density and CH_4 density profiles from Vervack et al. (2004) derived from the solar occultation measured by Voyager 1/UVS. The HASI-derived N_2 profile and the profile from the UVIS/EUV-stellar occultation during T21 are above all the other profiles shown. These two are the only profiles measured close to Titan northern winter season, or half way to the Vernal Equinox, all the others were measured close to Titan Vernal Equinox. The UVS profile agrees well with the T26 UVIS/EUV-solar profile, measured almost 27 years later and at higher latitude. Although comparisons with the HASI or the UVS profile could provide clues when analyzing seasonal or long term variations in the atmosphere, no firm conclusions can be made from these specific comparisons.

Due to the variety of factors determining the temporal and geographical behavior of the atmosphere, it is difficult to establish a criterion to compare different profiles from different observations. Moreover, comparison of results from different experiments is complicated by differences in retrieval methods or uncertainties in instrument calibration. Nevertheless, the variability of Titan's upper atmosphere is undeniable.

4.4. Thermospheric Temperature and Temperature Variability

Average temperature in the upper atmosphere was calculated from the N_2 number densities with the procedures described in Section 2.2. The altitude range used for the calculation of temperature is indicated by the horizontal dotted lines shown in Figure 7. The temperatures derived from the 8 observations analyzed are shown in Table 1. It is worth noting that temperatures for the upper atmosphere were not measured before for most of the flybys analyzed here. We derived two temperatures from the occultation $T62_{egress}$ (see Section 2.2). The lower limit we obtain is (135 ± 2) K, the 'low altitude temperature' we obtain is (179 ± 9) K. The fact that this temperature was calculated from only the six lower values in the profile (Figure 7) has to be kept in mind when comparing this temperature with that from other observations.

The global average temperature and temperatures for flybys T26 and T58 are shown in Table 4, together with equivalent results from previous work. We calculated, as a weighted average, a global temperature of (150 ± 1) K, the standard deviation of the set of 8 values used is 24 K. These values changed to (149 ± 1) K and 22 K if $T62_{egress}$ is not considered. Our global temperature is consistent with the global temperatures shown in Table 4 and derived from INMS data (the value from Westlake et al. (2011) is within 3-σ from our value). It should be noted that our global average was determined from only 8 values. The other references in Table 4 use temperatures determined from several tens of flybys.

Interestingly, our temperature for flyby T58 is remarkably cold in comparison with the others in Table 4. It should be noted that the INMS measurements correspond to the mid/high southern latitudes while our measurement corresponds to 86 N, nearly at the north pole. For T26, on the contrary, our temperature is consistent with the ones presented in the table. Using a similar

Table 3. Temporal and geographical characteristics for the set of measurements shown in Figure 10.

Measurement	Time (mm/yy)	Close to Titan Season	Solar Activity	Latitude[a] (deg)	Longitude[a] (deg W)
UVIS T53 solar occ.	04/09	Vernal Equinox	Min.	-21 – -29	237
UVIS T53 star occ.	04/09	Vernal Equinox	Min.	38 – 39	294 – 308
UVIS T26 solar occ.	03/07	Vernal Equinox	Low	-76 – -77	41 – 29
UVIS T58 solar occ.	07/09	Vernal Equinox	Low	87 – 85	240 – 237
UVIS T21 star occ.	12/06	North. win./Ver. Eq.	Low	-35	116
HASI	01/05	Northern winter	Low	-9.5	186.2
UVS solar occ.	11/80	Vernal Equinox	High	4	107
INMS T26	03/07	Vernal Equinox	Low	31.7	358
INMS T58	07/09	Vernal Equinox	Low	-52.2	178

[a]For INMS observations, the latitude and longitude correspond to closest approach.

Table 4. Global temperature and temperatures for specific flybys.

Reference	This Work	Cui et al. (2009)	Westlake et al. (2011)	Snowden et al. (2013)
Global average (K)	150 ± 1	151.0 ± 0.5	153.0 ± 1.2	150.7 ± 4.2
T26 (K)	139 ± 5	···	142.9 ± 1.3	141.0 ± 6.5 / 138.2 ± 4.9[b]
T58 (K)	113 ± 3	···	∼140[a]	156.5 ± 5.5 / 145.6 ± 6.3[b]
Instrument	UVIS	INMS	INMS	INMS

[a]Approximate value from Figure 4 in the reference.

[b]Inbound/outbound leg, high altitude density level.

technique as the one presented here, Kammer et al. (2013) derived averaged temperature for the upper atmosphere from the N_2 profiles measured during UVIS/EUV-stellar occultations. Their value for T21 is ($149.6\ ^{+13.6}_{-11.6}$) K, which falls between the 163 K we derived from T10 and the 139 K we derived from T26. Also fitting isothermal profiles to the nitrogen densities, Vervack et al. (2004) found a thermospheric temperature of (153 ± 5) K with no variation, taking into account the uncertainties, for the ingress and egress occultations measured by Voyager 1/UVS in 1980. The comparison of values from individual flybys makes sense only when factors such as location and time are also taken into account, as they affect the thermospheric temperature. Nevertheless, the average temperature that we retrieved from Cassini/UVIS solar occultations agrees with all previous measurements, based either on Cassini/INMS, Voyager/UVS or Cassini/UVIS stellar occultations. The range of temperatures we obtained also agrees with the previously determined range of temperatures, including the peculiarly cold and warm flybys, thus confirming the remarkable variability that the INMS has observed.

Variability is important in Titan's atmosphere. Measured temperatures can vary roughly between 100 - 200 K (see for example Snowden et al. 2013) from flyby to flyby. The combined effects from the different variables affecting the behavior of the atmosphere (day/night, season, position in the magnetosphere, etc.) are complex and the variables cannot be easily decoupled, especially when dealing with limited data sets with poor statistics and easily biased by outliers, like in the present case. Nevertheless, an evident correlation of our 8 temperatures with some of those variables could suggest a trend in behavior. We present next the temperatures as a function of several variables, concentrating first in the horizontal variability and, later, in the temporal variability.

Figure 11 shows the temperatures from all the solar occultations as a function of latitude (left) and longitude (right). The temperatures decrease from the equator to the north pole. This trend does not repeat in the southern hemisphere, where mid-latitude temperatures from the flybys T10 and $T62_{egress}$ are warmer than that derived for a high-latitude from the T53 flyby. We remind however that the lower limit we derived for the temperature for $T62_{egress}$ is 135 K. No correlation with longitude is evident from the right plot in Figure 11. In particular, three different values spanning almost the whole range of temperature measured are concentrated in the

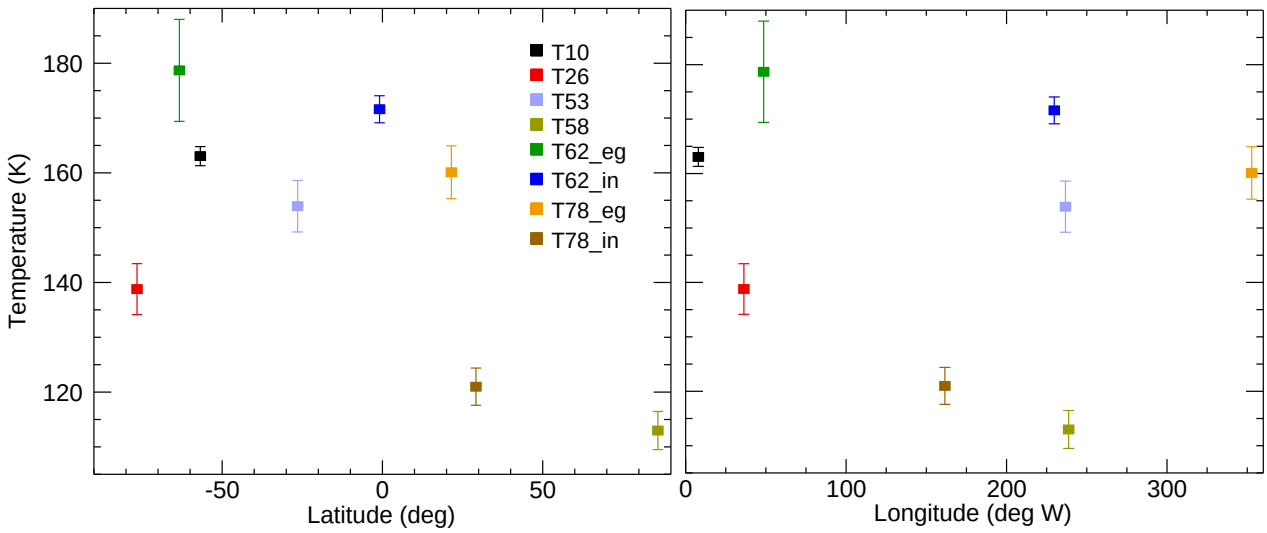

Fig. 11.— Upper atmospheric temperatures as a function of latitude (left) and longitude (right) for the solar occultations analyzed.

region 230° - 240° W. Cui et al. (2009) studied composition and thermal structure of the upper atmosphere based on the analysis of INMS data from 15 Titan flybys spanning 2.5 years, from April 2005 till November 2007. They showed that the equatorial region in Titan's thermosphere appears to be warmer than the north polar region. Cui et al. (2009) give a temperature difference between the equator and north pole of ∼10 K, while the difference between our northernmost temperature and the one closer to the equator is of about 60 K. The restricted sampling of the available INMS data at the time of publication did not allow Cui et al. (2009) to make a firm conclusion on the realistic horizontal variations. Later work relying on a much larger number of INMS measurements include that of Westlake et al. (2011) (29 flybys from 2004 till 2009) and that of Snowden et al. (2013) (32 flybys from 2006 till 2010). Both have pointed to the same trend — that the north polar region tends to have the lowest temperatures while the equator has the warmest temperatures. This trend does not appear to hold in the southern hemisphere, however, where the mid-latitude region tend to be warmer than the low latitude region. This is consistent with our measurements. Snowden et al. (2013) found an insignificant difference in the temperature calculated for different longitude regions.

The lack of sufficient data points prevents firm conclusions about horizontal variability.

Although this is particularly true for our sparse sampling of the atmosphere from solar occultations, we present results for flybys not included in the studies cited above, so our works are complementary. The data suggest that there is no detectable correlation with longitude. On the other hand the north pole might be colder than the equator or southern latitudes, this calls for further attention to this latitudinal trend in thermospheric temperatures.

Titan's atmosphere presents also temporal variability. The temperatures from the solar occultations correspond to either the morning or evening terminator (See Figure 12). Measurements in the morning terminator could be considered representative of an atmosphere coming out the night, and those from the evening terminator representative of an atmosphere coming from a day period. No day/night differences are evident in our results, measurements in the evening terminator span across almost the whole range of temperature measured. Mueller-Wodarg et al. (2000), using a 3-D General Circulation Model (GCM) of Titan's thermosphere, found diurnal and hemispheric variability of up to 10 - 20 K in thermospheric temperatures, resulting from solar EUV heating; the variability was largest above 1300 km. On the contrary, Cui et al. (2009) found the nightside to be warmer than the dayside. A similar trend was found in Westlake et al. (2011) and Snowden et al. (2013); although the day/night temperature difference found by the latter is smaller than in previous calculations, and their final conclusion is that no relevant dependence on local time can be derived from the observations, in agreement with our results form the UVIS occultations.

Figure 12 shows the measured temperatures as a function of time, the vertical line showing Titan's Vernal Equinox on 2009 August 11. No correlation with time or Solar activity is apparent, as neither is from the temporal trend shown in Westlake et al. (2011). Snowden et al. (2013) state that the average temperature of Titan's thermosphere may have decreased by about 10 - 15 K around mid-2007, or around T32. However, the data from the solar occultations are not sufficient to establish any long term temperature trends in the data.

Titan's thermospheric temperature vary considerably as a function of time and location, yet, this variability might result from a combined effect of the variables considered here, and taking only one of them at a time could be misleading.

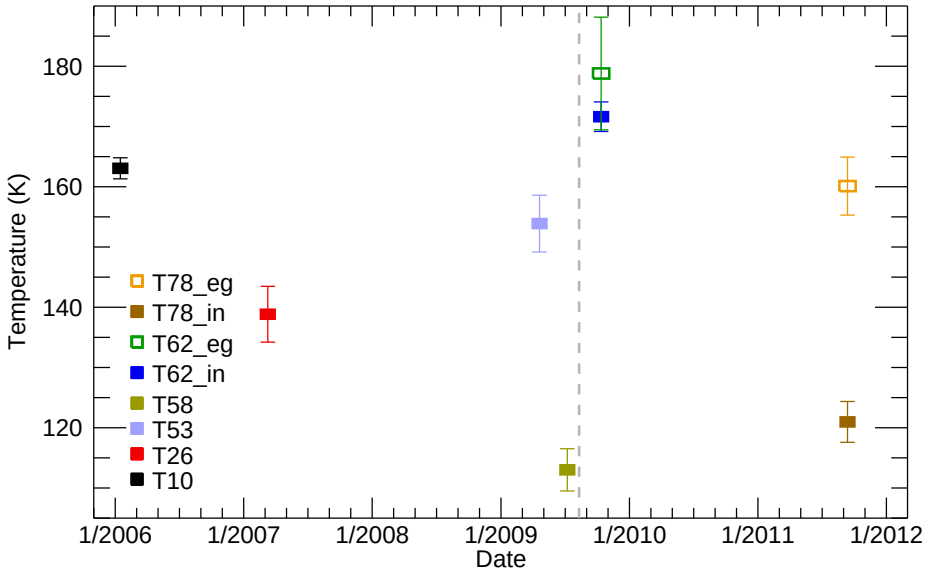

Fig. 12.— Upper atmospheric temperatures as a function of time, corresponding to the morning terminator (open symbols) or the evening terminator (closed symbols). The vertical line shows Titan's Vernal Equinox in August 2009. Date format: M/YYYY.

5. SUMMARY AND CONCLUSIONS

We analyzed 8 UVIS/EUV-solar occultations by Titan's atmosphere, taking place between flybys T10 and T78, for which data are available in the PDS archive. We developed methods to correct the data from background contamination, and wavelength shifts due to pointing instabilities. In some cases, the wavelength re-calibration implemented permitted the analysis of observations that, without the corrections, would be useless for retrieving the atmospheric composition.

From the solar occultations we retrieved the density profiles of CH_4 at altitudes of 850-1300 km, and density profiles of N_2 at altitudes of 1100-1600 km. The profiles include oscillations that might be indicative of atmospheric waves (Koskinen et al. 2011; Snowden et al. 2013) or, in case of small scale fluctuations, artifacts from the inversion procedure. We used the density profiles to calculate the CH_4 mole fractions. The results come with relatively large uncertainties, but they appear to confirm the variability of CH_4 mixing ratio and the variability of methane escape observed in the INMS data (Cui et al. 2012; Westlake et al. 2014).

The data presented here complement measurements from other instruments. In Section 4.3 we compared our CH_4 profiles and N_2 profiles with those from other observations and instruments. These data cover a wide range of locations and times. We stress the difficulty of comparing the different profiles, which are affected by different factors determining the undeniable variability of the atmosphere. We addressed this variability in terms of an analysis of number density variation and thermospheric temperature variation. The data set of solar occultations analyzed cover different latitudes and longitudes, in many cases corresponding to times and locations for which no experimental thermospheric temperatures were available in the bibliography. The previously observed variability of CH_4 abundances and N_2 abundances in the upper atmosphere is confirmed by the difference between profiles from different solar occultations, or among the profiles presented here and those derived from other observations at different times/locations. In particular, in agreement with INMS observations, we observed an overall tendency of decreasing abundance with time for both species, the abundances measured late in the Cassini mission being smaller than those measured early in the mission.

The upper atmosphere temperature was calculated for each of the 8 solar occultations analyzed. Our global mean temperature of (150 ± 1) K agrees with previous measurements by different instruments. The range of temperatures we obtained agrees with the previously determined range of temperatures, including the peculiarly cold and warm flybys. Analysis of the eight temperatures as a function of different geographical and temporal variables showed no evident correlation with longitude, local time or season. The data suggest that the north pole might be colder than the equator or southern latitudes, although the lack of sufficient data points prevents firm conclusions in this regard.

The variability in the densities and in thermospheric temperature is undeniable. However, the sampling of the occultations data set is restricted, uncertainties from different profiles overlap at high altitudes, and different locations are blended in the statistical analysis of number densities. Thus, the general trends presented should be interpreted with caution. Moreover, we stress the fact that the variability observed might be caused by a complex combination of the variables considered (or other not considered) in the analysis of temperature variability, making these kind of studies very delicate.

In summary, the number density profiles, mole fraction profiles, and temperatures presented provide new observational data to constrain the studies of composition, temperature, and dynamics of Titan's upper atmosphere. Furthermore, Cassini arrived at the Saturnian system in 2004 and the mission is planned to be continued till 2017, so more observations will be available to deepen the study of variability and long-term changes in Titan's atmosphere.

We acknowledge the financial support from the French Space Agency (Centre National d'Études Spatiales, CNES). TTK was supported by the NASA CDAPS grant NNX14AD51G.

REFERENCES

Acton, C. H. 1996, Planet. Space Sci., 44, 65

Broadfoot, A., et al. 1977, Space Sci. Rev., 21, 183

Capalbo, F. J. 2014, PhD thesis, University of Paris Est

Capalbo, F. J., Bénilan, Y., Yelle, R. V., et al. 2013, ApJ, 766, L16

Cui, J., Yelle, R. V., Strobel, D. F., et al. 2012, J. Geophys. Res., 117, E11006

Cui, J., Yelle, R. V., Vuitton, V., et al. 2009, Icarus, 200, 581

Fulchignoni, M., et al. 2005, Nature, 438, 785, doi:10.1038/nature04314

García-Comas, M., López-Puertas, M., Funke, B., et al. 2011, Icarus, 214, 571

Kameta, K., Kouchi, N., Ukai, M., & Hatano, Y. 2002, J. Electron Spectrosc. Relat. Phenom., 123, 225

Kammer, J., Shemansky, D., Zhang, X., & Yung, Y. 2013, Planet. Space Sci., 88, 86 , atmospheres, Magnetospheres and Surfaces of the outer planets, their satellites and ring systems: Part {IX}

Koskinen, T., Yelle, R., Snowden, D., et al. 2011, Icarus, 216, 507

Lara, L. M., Lellouch, E., Lopez-Moreno, J. J., & Rodrigo, R. 1996, J. Geophys. Res., 101, 23261

LASP. 2014, Cassini UVIS User's Guide., Laboratory for Atmospheric and Space Physics, Boulder, CO, http://pds-rings.seti.org/cassini/uvis/index.html

Lavvas, P., Sander, M., Kraft, M., & Imanaka, H. 2011, ApJ, 728, 80

Lewis, B. R., Heays, A. N., Gibson, S. T., Lefebvre-Brion, H., & Lefebvre, R. 2008, J. Chem. Phys., 129, 10.1063/1.2990656

Magee, B. A., Waite, J. H., Mandt, K. E., et al. 2009, Planet. Space Sci., 57, 1895

Mueller-Wodarg, I., Yelle, R., Mendillo, M., Young, L., & Aylward, A. 2000, J. Geophys. Res., 105, 20833

Mueller-Wodarg, I. C. F., Yelle, R. V., Cui, J., & Waite, J. H. 2008, J. Geophys. Res., 113, E10005

Samson, J. A. R., Masuoka, T., Pareek, P. N., & Angel, G. C. 1987, J. Chem. Phys., 86, 6128

Sarani, S. 2009, in Proceedings of the AIAA Guidance, Navigation, and Control Conference (New York: Am. Inst. of Aeronaut. and Astronaut.), abstr. 5763

Smith, G. R., & Hunten, D. M. 1990, Reviews of Geophysics, 28, 117

Smith, G. R., Strobel, D. F., Broadfoot, A. L., et al. 1982, J. Geophys. Res., 87, 1351

Snowden, D., Yelle, R., Cui, J., et al. 2013, Icarus, 226, 552

Stevens, M. H., Evans, J. S., Lumpe, J., et al. 2015, Icarus, 247, 301

Stevens, M. H., Gustin, J., Ajello, J. M., et al. 2011, J. Geophys. Res., 116, A05304

Strobel, D. F., Summers, M. E., & Zhu, X. 1992, Icarus, 512

Teolis, B., Niemann, H., Waite, J., et al. 2015, Space Sci. Rev., 1

Vervack, J. R. J., Sandel, B. R., & Strobel, D. F. 2004, Icarus, 170, 91

Waite, J.H., J., Niemann, H., Yelle, R., et al. 2005, Science, 308, 982

Westlake, J. H., Bell, J. M., Waite, J. H., et al. 2011, J. Geophys. Res., 116, A03318

Westlake, J. H., Waite, J. H., Bell, J. M., & Perryman, R. 2014, J. Geophys. Res., 119, 8586

Yelle, R. V., Cui, J., & Mueller-Wodarg, I. C. F. 2008, J. Geophys. Res., 113, E10003

Yelle, R. V., Strobell, D. F., Lellouch, E., & Gautier, D. 1997, in Huygens: Science, Payload and Mission, Proceedings of an ESA conference, ed. A. Wilson, 243 – 256, eSA SP-1177

Yung, Y., Allen, M., & Pinto, J. 1984, ApJS, 55, 465